



EDGEWOOD CHEMICAL BIOLOGICAL CENTER

U.S. ARMY RESEARCH, DEVELOPMENT AND ENGINEERING COMMAND
Aberdeen Proving Ground, MD 21010-5424

ECBC-TR-1166

INFRARED COMPLEX OPTICAL CONSTANTS OF GB, GF, HD, HN1, AND VX

Clayton S.C. Yang

BATTELLE MEMORIAL INSTITUTE
Aberdeen, MD 21001-1228

Alan C. Samuels
Ronald W. Miles, Jr.

RESEARCH AND TECHNOLOGY DIRECTORATE

Barry R. Williams
Melissa S. Hulet

LEIDOS
Gunpowder, MD 21010-0068

April 2014

Approved for public release; distribution is unlimited.



Disclaimer

The findings in this report are not to be construed as an official Department of the Army position unless so designated by other authorizing documents.

REPORT DOCUMENTATION PAGE				Form Approved OMB No. 0704-0188																			
Public reporting burden for this collection of information is estimated to average 1 hour per response, including the time for reviewing instructions, searching existing data sources, gathering and maintaining the data needed, and completing and reviewing this collection of information. Send comments regarding this burden estimate or any other aspect of this collection of information, including suggestions for reducing this burden to Department of Defense, Washington Headquarters Services, Directorate for Information Operations and Reports (0704-0188), 1215 Jefferson Davis Highway, Suite 1204, Arlington, VA 22202-4302. Respondents should be aware that notwithstanding any other provision of law, no person shall be subject to any penalty for failing to comply with a collection of information if it does not display a currently valid OMB control number. PLEASE DO NOT RETURN YOUR FORM TO THE ABOVE ADDRESS.																							
1. REPORT DATE (DD-MM-YYYY) XX-04-2014		2. REPORT TYPE Final		3. DATES COVERED (From - To) Mar 2011 – Jul 2012																			
4. TITLE AND SUBTITLE Infrared Complex Optical Constants of GB, GF, HD, HN1, and VX				5a. CONTRACT NUMBER																			
				5b. GRANT NUMBER																			
				5c. PROGRAM ELEMENT NUMBER																			
6. AUTHOR(S) Yang, Clayton S.C. (Battelle Memorial Institute); Samuels, Alan C.; Miles, Ronald W. Jr. (ECBC); Williams, Barry R.; and Hulet, Melissa S. (Leidos*).				5d. PROJECT NUMBER CA09DET503H																			
				5e. TASK NUMBER																			
				5f. WORK UNIT NUMBER																			
7. PERFORMING ORGANIZATION NAME(S) AND ADDRESS(ES) Battelle Memorial Institute, 1204 Technology Drive, Aberdeen, MD 21001-1228 Director, ECBC, ATTN: RDCB-DRD-P, APG, MD 21010-5424 Leidos*, P.O. Box 68, Gunpowder, MD 21010-0068				8. PERFORMING ORGANIZATION REPORT NUMBER ECBC-TR-1166																			
9. SPONSORING / MONITORING AGENCY NAME(S) AND ADDRESS(ES)				10. SPONSOR/MONITOR'S ACRONYM(S)																			
				11. SPONSOR/MONITOR'S REPORT NUMBER(S)																			
12. DISTRIBUTION / AVAILABILITY STATEMENT Approved for public release; distribution unlimited.																							
13. SUPPLEMENTARY NOTES *A portion of Science Applications International Corporation became Leidos in 2013.																							
14. ABSTRACT This report discusses the complex optical constants ($\hat{n} = n + ik$) of several nerve agents and vesicants in the mid-infrared region. The measurements were made using infrared variable-angle spectral ellipsometry. Ellipsometry with attenuated total reflection permits the determination of both optical constants in a single measurement. This contrasts with the more traditional methods of obtaining the optical constants using transmission measurements that required the real refractive index to be extrapolated outside of the measured range.																							
15. SUBJECT TERMS <table border="0"> <tr> <td>Refractive index</td> <td>Absorptivity coefficient</td> <td>k index</td> </tr> <tr> <td>Ellipsometry</td> <td>Imaginary refractive index</td> <td>Infrared</td> </tr> <tr> <td>Transmission</td> <td>Nitrogen mustard (HN1)</td> <td>Reflection</td> </tr> <tr> <td>Blister agent</td> <td>Cyclosarin (GF)</td> <td>Sarin (GB)</td> </tr> <tr> <td>Nerve agent</td> <td>Mustard agent (HD)</td> <td>VX</td> </tr> <tr> <td>Complex optical constants</td> <td colspan="2">Infrared variable-angle spectral ellipsometer (IR-VASE)</td> </tr> </table>						Refractive index	Absorptivity coefficient	k index	Ellipsometry	Imaginary refractive index	Infrared	Transmission	Nitrogen mustard (HN1)	Reflection	Blister agent	Cyclosarin (GF)	Sarin (GB)	Nerve agent	Mustard agent (HD)	VX	Complex optical constants	Infrared variable-angle spectral ellipsometer (IR-VASE)	
Refractive index	Absorptivity coefficient	k index																					
Ellipsometry	Imaginary refractive index	Infrared																					
Transmission	Nitrogen mustard (HN1)	Reflection																					
Blister agent	Cyclosarin (GF)	Sarin (GB)																					
Nerve agent	Mustard agent (HD)	VX																					
Complex optical constants	Infrared variable-angle spectral ellipsometer (IR-VASE)																						
16. SECURITY CLASSIFICATION OF:			17. LIMITATION OF ABSTRACT	18. NUMBER OF PAGES	19a. NAME OF RESPONSIBLE PERSON																		
a. REPORT U	b. ABSTRACT U	c. THIS PAGE U	UU	48	Renu B. Rastogi																		
					19b. TELEPHONE NUMBER (include area code) (410) 436-7545																		

Blank

PREFACE

The work described in this report was performed under the direction of the Joint Science and Technology Office, project number CA09DET503H. This work was started in March 2011 and completed in July 2012.

The use of either trade or manufacturers' names in this report does not constitute an official endorsement of any commercial products. This report may not be cited for purposes of advertisement.

This report has been approved for public release.

Acknowledgments

The authors thank the late Dr. Ngai Wong (Defense Threat Reduction Agency, Joint Science and Technology Office) for his support and encouragement of this work.

Blank

CONTENTS

1.	INTRODUCTION	1
2.	EXPERIMENTAL SECTION	4
2.1	Vertical ATR IR-Variable-Angle Spectral Ellipsometer (VASE) Laboratory	4
2.2	Ellipsometry Theory	4
2.3	ATR IR-VASE Liquid-Sampling Assembly	5
2.4	Instrument Parameters	7
2.5	Compound Details	7
3.	RESULTS AND DISCUSSION	9
3.1	Complex Refractive Index of GB	9
3.2	Complex Refractive Index of GF.....	15
3.3	Complex Refractive Index of HD	18
3.4	Complex Refractive Index of HN1	24
3.5	Complex Refractive Index of VX.....	27
4.	CONCLUSIONS.....	31
	LITERATURE CITED	33
	ABBREVIATIONS	35

FIGURES

1.	Synthetically generated spectrum with peaks at 800 and 500 cm^{-1} (left) and values of n generated from a K-K transformation (right)	3
2.	J.A. Woollam Company vertical ATR IR-VASE installed in chemical agent fume hood (left) and schematic showing principal system components (right).	4
3.	ATR IR-VASE liquid-sampling assembly. Key components are highlighted.	6
4.	Complex refractive index of liquid GB: n (top) and k (bottom).	9
5.	Linear absorptivity coefficient (K) of liquid GB.	10
6.	Lorentzian peak (full width at half height of 20 cm^{-1}) in a synthetically generated K spectrum (red trace), contrasted with the same peak in the k spectrum computed with eq 1 (blue trace).	12
7.	Complex refractive indices of GB from the ECBC (blue trace) and PNNL (black trace) databases	13
8.	Imaginary refractive indices of GB from SRI (blue trace), ECBC (red trace), and PNNL (black trace) ellipsometry data	14
9.	Baselines in k spectra of GB from ECBC (blue trace) and PNNL (black trace).	15
10.	Complex refractive index of liquid GF: n (top) and k (bottom).	16
11.	Linear absorptivity coefficient (K) of liquid GF.	17
12.	Complex refractive index of GF from ECBC (blue trace) and PNNL (black trace) databases. The spectra are qualitatively and quantitatively similar.	18
13.	Data spacing in the Ψ and Δ of HD, as recorded by the ellipsometer software	19
14.	Imaginary refractive index of HD from ellipsometry measurements at ECBC: original data with variable spacing (blue trace) and spectrum after interpolating with the Matlab pchip algorithm (red trace).	20
15.	Complex refractive index of liquid HD: n (top) and k (bottom).	21
16.	Linear absorptivity coefficient of liquid HD.	21
17.	Complex refractive index of HD from ECBC (blue trace) and the PNNL database (black trace)	23
18.	Complex refractive index of liquid HN1: n (top) and k (bottom).	25
19.	Linear absorptivity coefficient of liquid HN1.	25
20.	Complex refractive index of liquid VX: n (top) and k (bottom).	28
21.	Linear absorptivity coefficient of liquid VX.	28
22.	Complex refractive index of VX from ECBC (blue trace) and the PNNL database (black trace)	31
23.	Imaginary refractive index of VX from ECBC (blue trace) and the PNNL database (black trace) expanded to the region near 1300 cm^{-1}	31

TABLES

1.	Instrument Parameters Used in Ellipsometry Measurements	7
2.	Chemical Agents Studied for This Report	8
3.	Chemical Agent Structures and Physical Properties	8
4.	Positions and Intensities of Selected Peaks in k and K Spectra of GB	10
5.	Positions and Values of Selected Maxima and Minima in Real Refractive Index of GB	11
6.	Positions and Intensities of Selected Peaks in k and K Spectra of GF	17
7.	Positions and Values of Selected Maxima and Minima in Real Refractive Index of GF	18
8.	Positions and Intensities of Selected Peaks in k and K Spectra of HD	22
9.	Positions and Values of Selected Maxima and Minima in Real Refractive Index of HD	22
10.	Integrated Areas in k Index from PNNL and ECBC Measurements of HD	24
11.	Positions and Intensities of Selected Peaks in k and K Spectra of HN1	26
12.	Positions and Values of Selected Maxima and Minima in Real Refractive Index of HN1	26
13.	Positions and Intensities of Selected Peaks in k and K Spectra of VX	29
14.	Positions and Values of Selected Maxima and Minima in Real Refractive Index of VX	29

Blank

INFRARED COMPLEX OPTICAL CONSTANTS OF GB, GF, HD, HN1, AND VX

1. INTRODUCTION

There is an ongoing need in the standoff detection communities for complex refractive index data from chemical and biological warfare agents and related materials in the infrared (IR) spectra. Understanding their optical properties is essential for the development of the ability to remotely detect these agents in the condensed phase. For isotropic materials such as liquids, one complex parameter, ($\hat{n} = n + ik$), the index of refraction (where \hat{n} in this case denotes a complex quantity), is sufficient to describe the responses of these materials to external optical (electromagnetic) fields. In this complex parameter:

- The optical constants n and ik represent the optical properties of a material in terms of how an electromagnetic wave will propagate in the material.
- The value n , the real part of the refractive index, is related to the phase change of the applied electromagnetic field due to the interaction of light with the material.
- The value ik , the imaginary part of the refractive index, is proportional to the degree to which the applied electromagnetic field is attenuated (by absorption) by the material.

If the optical constants are known, the intensity of the reflected and/or transmitted light through the bulk liquid can be predicted accurately.

The liquid-phase optical constants of a number of chemical agents have traditionally been investigated using transmission through liquid cells. Those measurements are usually difficult to make because the high optical densities of the compounds in the IR region require liquid cells with paths of only a few micrometers in length. An early approach by personnel at the Southern Research Institute (SRI; Birmingham, AL) attempted to overcome this difficulty by analyzing dilute solutions of the agents in solvents.¹ However, because of solvent/solute interactions, spectra obtained using this method often exhibited shifts in frequencies and intensities of absorption bands. A refinement of the transmission technique was undertaken by personnel at the Pacific Northwest National Laboratory (PNNL; Richland, WA) and Dugway Proving Ground (DPG, UT)² who distributed an updated database of the optical constants of the agents in electronic form.³ The fabrication of liquid cells with path lengths as short as 2.6 μm permitted the analysis of agents in neat form without saturating the strongest absorption bands. Common to transmission methods, however, was the limitation that only the linear absorption coefficient, K , [$K(\tilde{\nu}) = A_{\log 10}(\tilde{\nu})\text{cm}^{-1}$] could be obtained directly.

A simple mathematical relationship relates K to the dimensionless absorption index $(ik)^*$

$$ik(\nu) = \frac{\ln(10) K(\nu)}{4\pi\nu} \quad (1)$$

However, deriving the real refractive index, n , from the absorption index (or extinction coefficient), k , requires connecting the real and imaginary parts of a complex function. Traditionally this has been accomplished through the Kramers-Kronig (K-K) relationship

$$n(\nu_i) = \frac{2}{\pi} P \int_0^\infty \frac{\nu k(\nu)}{\nu^2 - \nu_i^2} d\nu + n(\infty) \quad (2)$$

The integral in eq 2 represents a $\Delta n(\nu_i)$ that, when summed with the scalar quantity $n(\infty)$, computes the real refractive index part of the complex optical constant at the frequency being evaluated. There are inherent difficulties in solving eq 2. First, the values of k and n are not available from 0 to ∞ . Furthermore, a pole exists at $\nu_i = \nu_j$. Various schemes have been used to approximate the derivative. In general, they use a finite range of measured values $[k(\nu_i) \text{ to } k(\nu_n)]$, a known high wavenumber anchor point for n to substitute for $n(\infty)$ that is as close as possible to ν_n , and an assumption that $k = 0$ outside the measured range.

Two primary errors can manifest themselves and cause deviations in the calculated values of n . First, nonzero values of k outside of the wings of the measured range introduce errors in the calculation of $\Delta n(\nu_i)$. The fundamental, hence the strongest, absorption features in IR spectra are typically observed at frequencies less than 4000 cm^{-1} . The influence of unobserved absorption bands on the absorption index spectrum (and thereby the real refractive index) above this frequency is typically small. On the other hand, the usual lower-frequency cutoff of a mid-IR spectrometer is near 600 cm^{-1} for a mercury-cadmium-telluride (MCT) detector or near 400 cm^{-1} for a deuterated triglycine sulfate (DTGS), which are above the frequencies of some fundamental bands. Unobserved bands at frequencies less than the cutoff contribute a positive bias in the calculation of $\Delta n(\nu_i)$. The effects of such induced errors are shown in Figure 1. The plot on left side of the figure represents a synthetic Lorentzian spectrum with peaks at 800 and 500 cm^{-1} . The right side of Figure 1 illustrates the results of two different K-K functions applied to the data: subtractive Kramers-Kronig (SKK) and MacLaurin Kramers-Kronig (MacLaurin KK). Ohta and Ishida showed that the SKK method appeared to improve the accuracy of the results when the K-K analysis was performed on data in which unobserved absorption features were present at frequencies below the cutoff of the data.⁴ The solid lines in Figure 1 represent the resulting calculated values of n , if the full range of k values from

* Note: In the literature, the imaginary refractive index is often called the *absorption index* or *extinction coefficient*, hereafter designated with a lowercase k . Compare the absorption index with the linear absorption coefficient, K , which is expressed as absorbance per unit of length, usually in centimeters. In other contexts, absorption coefficients (often designated by the Greek letter alpha [α]) are typically expressed as absorbance divided by the product of concentration and path length. Similarly, within the literature, the symbol for wavenumber is variously given the Greek letter ν , with or without a tilde: $\tilde{\nu}$ or ν . Equations 4 and 5 use the second form.

1200 to 400 cm^{-1} is used to compute the refractive index. The dashed lines in Figure 1 represent a plot of n , if only the k -index values from 1200 to 600 cm^{-1} are used. The real refractive index computed from the truncated data shows a positive bias in the region close to the low-frequency end of the range.

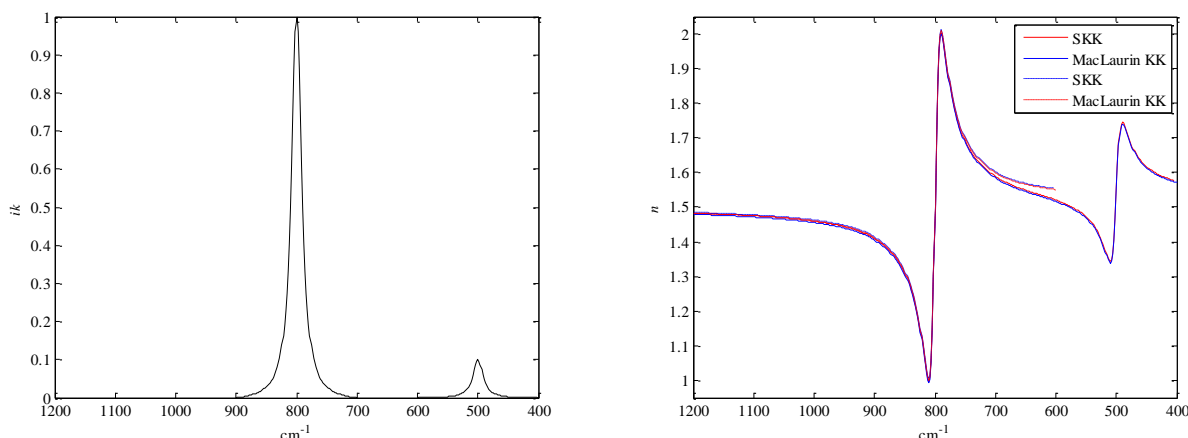


Figure 1. Synthetically generated spectrum with peaks at 800 and 500 cm^{-1} (left) and values of n generated from a K-K transformation (right). The unobserved peak in the truncated k -index data results in a positive bias in the computed values of n near the cutoff of the data at 600 cm^{-1} . The SKK transformation reduces, but does not eliminate, the bias.

The second potential source of deviation is evident in the right side of eq 2 because of the value of $n(\infty)$, which is a scalar. Errors in this quantity contribute an intercept bias when the result of the integral, $\Delta n(\nu_i)$, is summed with $n(\infty)$. Measured values of n for the chemical agents are generally available only for the sodium-D line (589.3 nm; 16,969.3 cm^{-1} [where the D stands for doublet]), which is well outside of the experimental range where the K-K transformations have been applied. For the analysis by PNNL, the anchor values of n for the nerve agents were extrapolated to 6500 cm^{-1} (1.538 μm) using the dispersion curves of four unrelated organophosphorous (OP) compounds.

Accurately determining the complex refractive indices of materials requires measuring not only the absolute intensity of the reflected light but also the relative change in both the intensity and phase between different polarizations of the reflected light. Ellipsometry, used in attenuated total reflection (ATR) geometry, is more accurate than other techniques because both optical constants of the complex index of refraction can be determined in a single ellipsometric measurement without the need for mathematical transformation. In particular, the values of the real refractive index obtained through ellipsometric measurements cannot be biased by unobserved absorption features outside of the measured range.

2. EXPERIMENTAL SECTION

2.1 Vertical ATR IR-Variable-Angle Spectral Ellipsometer (VASE) Laboratory

The experimental setup of our vertical ATR IR-VASE assembly is shown in Figure 2. The instrument was manufactured by J.A. Woollam Company, Inc. (Lincoln, NE). The IR-VASE consists of an IR light source (Bomem MB102 spectrometer; ABB; Zurich, Switzerland); a pair of linear polarizers and a compensator; a high-precision, θ to 2θ sample rotational stage; and an IR detector. Plane polarized light is reflected from the sample surface to produce an elliptically polarized reflected light.

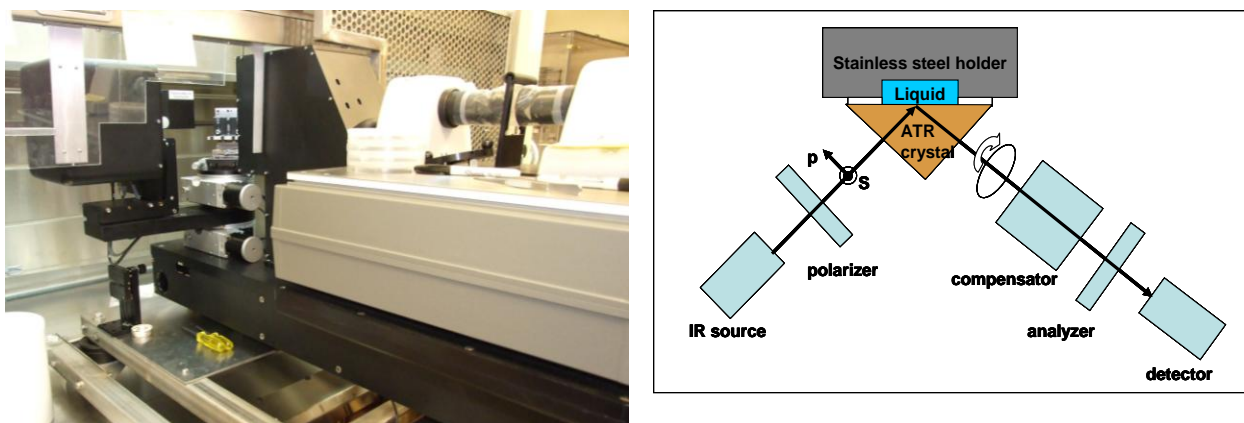


Figure 2. J.A. Woollam Company vertical ATR IR-VASE installed in chemical agent fume hood (left) and schematic showing principal system components (right).

Safety restrictions, necessary because of the toxicities of many of the compounds analyzed in our laboratory, required that these chemicals remain within engineering controls during analysis. The instrument was too large to accommodate all of its components within engineering controls; therefore, some assemblies extended out of the hood. For this reason, we worked with the Advanced Design and Engineering Division at the U.S. Army Edgewood Chemical Biological Center (ECBC) to fabricate and install a custom-designed sash that enabled the largest components of the system to be mounted on a bench outside of the hood, while ensuring that the sash enclosed all components that intersected the plane of the sash as tightly as possible. The instrument was installed in a fume hood equipped for chemical agent operations. With the instrument and associated equipment installed, the fume hood met all normal regulatory and safety requirements for such operations (e.g., airflow specifications, smoke testing, and monitoring).

2.2 Ellipsometry Theory

Ellipsometry measures the change in polarization state (intensity and phase) of light reflected from the surface of a material. An ellipsometer actually measures the values of the amplitude ratio, Psi (ψ), and the phase difference induced by the reflection, Delta (Δ). These

two real-number values are related to the ratio of complex Fresnel reflection coefficients, R_p and R_s , for p- and s-polarized light, respectively, by⁵

$$\tan \psi \exp(i\Delta) = \frac{R_p^*}{R_s^*} = \rho_{ps}^* \quad (3)$$

In other words,

$$\psi = \tan^{-1} \frac{|R_p|}{|R_s|} \quad (4)$$

and

$$\Delta = \delta_p - \delta_s = (\arg r_p - \arg r_s) \quad (5)$$

In the eqs 3 and 4, $\tan \psi$ is equal to the ratio of the reflectivity amplitude, expressed on the right side of eq 3 as the symbol for the complex reflectance ratio, ρ_{ps}^* . Geometrically, ψ can be interpreted as the angle between the axes of the reflected polarization ellipse and the linear polarization direction of the incident beam. The other ellipsometric parameter, Δ , is related to the ratio of polarization main axes of the ellipse. Physically, it is a measure of the phase shift, δ , between the s- and p-components of the light due to reflection from the sample. The optical constants of the sample can be determined from the Fresnel reflection coefficients for an interface of two media calculated from the measured ψ and Δ .

The ellipsometer in our laboratory, the IR-VASE, was a rotating-compensator ellipsometer (RCE). The RCE is an improved automatic ellipsometer that can be used to unambiguously determine the elliptical polarization phase angle (Δ) with a single measurement. Acquiring the optical constants in a single measurement reduces risk to the operators by eliminating the multiple filling and decontaminating operations that are required with a transmission technique.

2.3 ATR IR-VASE Liquid-Sampling Assembly

The ATR liquid-sampling assembly consisted of a stainless steel cell body with a cylindrical sample reservoir machined into the body, an ATR crystal, and a multidimensional alignment stage (Figure 3). The total liquid volume of the reservoir was approximately 0.9 mL. This sampling assembly was vertically mounted onto the high-precision, θ to 2θ sample rotational stage of the IR-VASE. For the sake of simplicity, the ATR crystal used in this study was a 45° ZnSe prism. The ATR crystal was affixed to the cell body with a stainless steel bar that was held in place with screws and aluminum shims at either end of the bar. A 0.1 mm polytetrafluoroethylene (PTFE) O-ring was used as a spacer between the crystal and the cell body to provide a leak-proof seal with no amalgam or other sealant. The assemblies could be reused after decontamination, rinsing, and drying. A laser-alignment assembly of the IR-VASE and the liquid-sampling assembly multidimension stage were used together to ensure

that the rotational axis of the liquid-sampling assembly was on the interfacial plane of the ATR crystal, perpendicular to the plane of incidence, and intersecting both incident and reflected IR beams on the ATR–sample assembly interface.

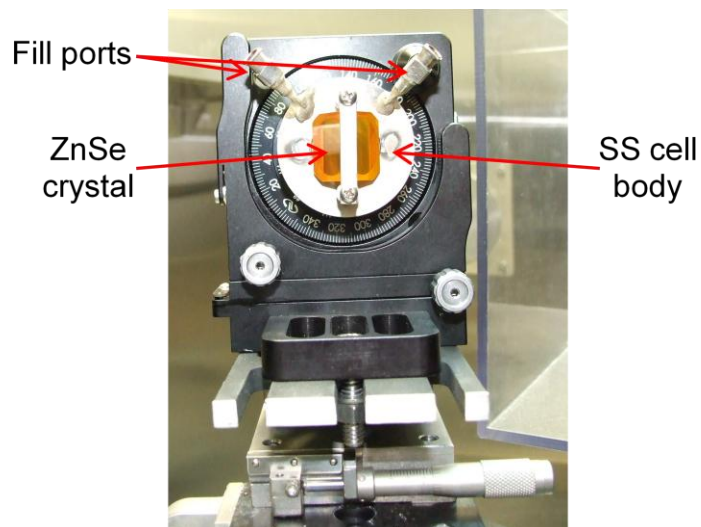


Figure 3. ATR IR-VASE liquid-sampling assembly. Key components are highlighted.

The liquid-sampling cell was assembled by seating the PTFE O-ring into a groove in the reservoir of the cell body, emplacing the ZnSe crystal over the reservoir such that the flange on the liquid side was seated into the groove, and securing the crystal in place using the bar, threaded posts, and screws. Securing the crystal could induce birefringence if excessive pressure was applied when the crystal was affixed to the body. This necessitated a balance between ensuring that sufficient pressure was applied to the crystal and O-ring to exclude leakage of the cell contents after filling, while also minimizing the risk of cracking or inducing birefringence in the ZnSe ATR crystal. During the early development of the method, we accomplished this by using a screwdriver to secure the screws slightly more than “finger tight” and then tightening the screws incrementally during the pressure test until leakage was minimized.

Using a torque driver, subsequent, more-systematic tests of the relationship between applied pressure, birefringence, and leakage rates indicated that applying 25 to 27 cNm to the screws appeared to provide a setting that was adequate to seal the cell without overstressing the crystal. Immediately before each measurement, we performed a pressure test on the assemblies to ensure the integrity of the seal and minimize the risk of contaminating either the operators or the instrument. The test was done using a digital manometer that was attached to the one of the fill ports of the cell with a plastic hose. A 100 cm³ plastic syringe was attached to the approximate midpoint of the hose through a plastic tee, along with a pinch clamp between the syringe and tee. This assembly enabled the application of differential pressure by either withdrawing or depressing the plunger of the syringe. The pressure check was then accomplished by (1) sealing the other fill port with a Teflon plug, (2) partially evacuating the cell by withdrawing the syringe plunger (typical practice was to apply approximately 400 Torr),

(3) noting a starting time and pressure reading, and (4) monitoring the pressure for 1 min. Our standard operating procedures specified that the change in pressure should be $\leq 10\%$ of the starting point after 1 min. In practice, typical pressure drops were much less than 10%.

The liquid-sampling assembly setup was calibrated before each measurement of the bulk optical properties of liquids. This calibration procedure determined the optical properties (especially birefringence) of the ATR crystal, which could be effectively represented by a model with several independent fitting parameters. Calibration was performed with no liquid in the assembly. Incorporating the calibration parameters that characterized the birefringence of the ATR crystal into the Fresnel model of the ATR crystal-liquid interface greatly improved the accuracy of the optical constant measurements of the liquids. The resolution of the calibration was required to be the same as that of the liquid measurement, which was 4 cm^{-1} in our studies. We acquired the calibration data at 10 scans per spectrum and averaged two spectra at a 45° incident angle.

2.4 Instrument Parameters

The instrument settings and other measurement parameters are listed in Table 1. All raw data files were archived to a network, enabling additional post-processing as needed.

Table 1. Instrument Parameters Used in Ellipsometry Measurements

Parameter	Value
Resolution	4 cm^{-1}
Zero fill	2
Final data spacing	2 cm^{-1}
Spectra/revolution	15
Scans/spectrum	20
Measure/cycles/angle	10
Bandwidth	$0.02\text{ }\mu\text{m}$
Minimum intensity ratio	2 to 5
Sample type	Isotropic
Input polarizer	45° with zone averaging
RCE analyzer	Single position

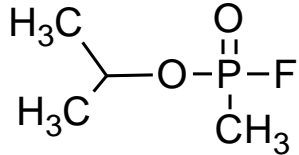
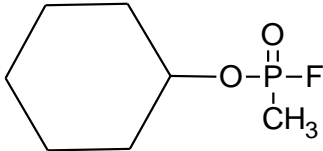
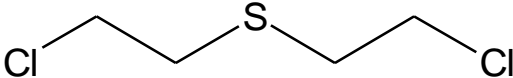
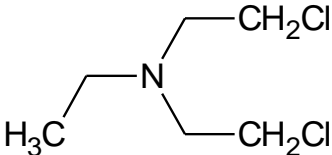
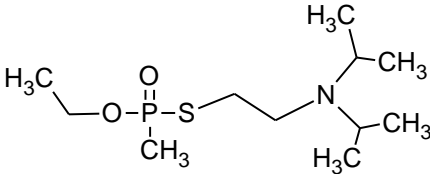
2.5 Compound Details

Chemical agent symbols, chemical names, and Chemical Abstracts Service Registry Numbers (CAS RNs) of the agents studied for this report are listed in Table 2. Structures and physical properties of the compounds are shown in Table 3. The data shown in Table 3 were extracted from Army Field Manual 3-11.9.⁶

Table 2. Chemical Agents Studied for This Report

Symbol	Chemical Name	CAS RN
GB	Isopropyl methylphosphonofluoridate	107-44-8
GF	Cyclohexyl methylphosphonofluoridate	329-99-7
HD	Bis-(2-chloroethyl) sulfide	505-60-2
HN1	Bis-(2-chloroethyl)ethylamine	538-07-8
VX	<i>O</i> -Ethyl- <i>S</i> -(2-diisopropylaminoethyl) methylphosphonothioate	50782-69-9

Table 3. Chemical Agent Structures and Physical Properties⁶

Chemical Structure	Physical Properties
	C ₄ H ₁₀ FO ₂ P FW: 140.09 Density: 1.0887 g/cm ³ at 25 °C VP: 2.48 Torr at 25 °C Lot: GB-U-5045-CTF-N Purity: 97.4 ± 0.6 mass %
	Formula: C ₇ H ₁₄ FO ₂ P FW: 180.16 Density: 1.1276 g/cm ³ at 25 °C VP: 0.00927 Torr at 25 °C Lot: GF-04-0046-81 Purity: >98%
	Formula: C ₄ H ₈ Cl ₂ S FW: 159.07 Density: 1.2685 g/cm ³ at 25 °C VP: 0.106 Torr at 25 °C Lot: HD-U-5032-CTF-N Purity: 98.0 ± 0.4 mol %
	Formula: C ₆ H ₁₃ Cl ₂ N FW: 170.08 Density: 1.09 g/cm ³ at 25 °C VP: 0.241 Torr at 25 °C Lot: HN1-9246-CTF-N Purity: >99%
	Formula: C ₁₁ H ₂₆ NO ₂ PS FW: 267.37 Density: 1.0083 g/cm ³ at 25 °C VP: 0.000878 Torr at 25 °C Lot: VX-U-7330-CTF-N Purity: 93.8 ± 0.4 mass %

FW: formula weight; VP: vapor pressure

3. RESULTS AND DISCUSSION

3.1 Complex Refractive Index of GB

The complex refractive index of GB is shown in Figure 4.

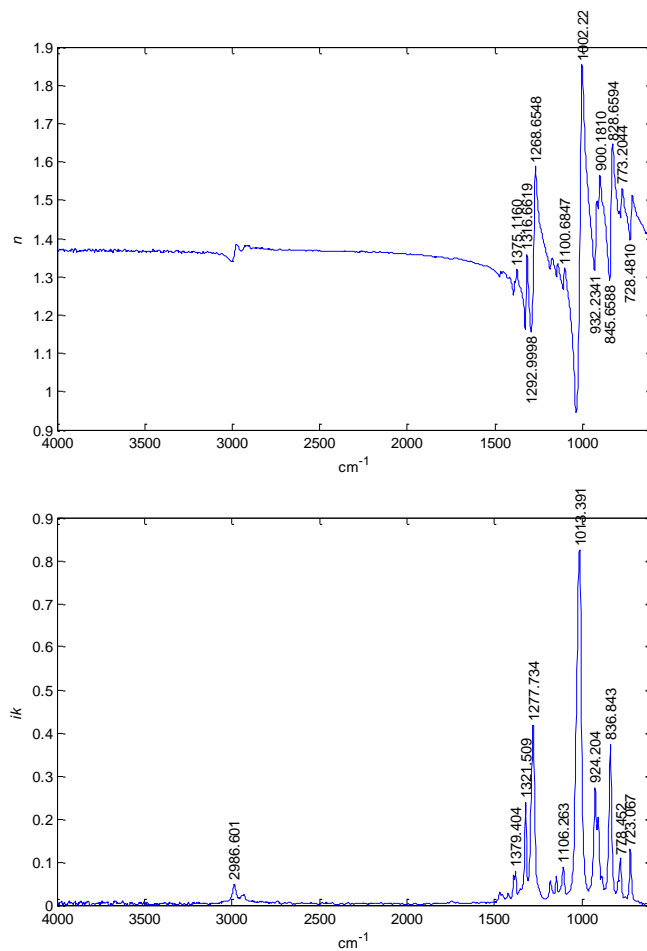


Figure 4. Complex refractive index of liquid GB: n (top) and k (bottom).

Figure 5 shows the linear absorptivity coefficient of the compound, which was computed by rearranging eq 1.

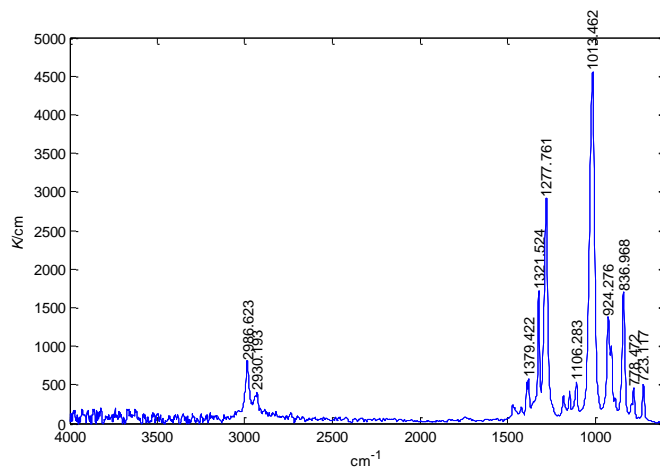


Figure 5. Linear absorptivity coefficient (K) of liquid GB.

Values of k and K at selected peak maxima are listed in Table 4. Values of the real refractive index at selected maxima and minima are shown in Table 5.

Table 4. Positions and Intensities of Selected Peaks in k and K Spectra of GB

k		K	
cm^{-1}	Intensity	cm^{-1}	Intensity
723.067	0.1290	723.117	509.1
778.452	0.1084	778.472	460.8
836.843	0.3718	836.968	1698.2
906.857	0.2031	906.921	1004.6
924.204	0.2730	924.276	1376.5
1013.391	0.8239	1013.462	4553.0
1106.263	0.0890	1106.283	537.7
1145.051	0.0666	1145.067	416.6
1179.968	0.0558	1180.008	359.6
1277.734	0.4177	1277.761	2912.7
1321.509	0.2379	1321.524	1715.3
2986.601	0.0495	2986.623	806.9

Table 5. Positions and Values of Selected Maxima and Minima in Real Refractive Index of GB

Position (cm ⁻¹)	Intensity
716.607	1.513
728.481	1.397
773.204	1.532
828.659	1.647
845.659	1.290
900.181	1.566
917.250	1.498
932.234	1.316
1002.223	1.854
1036.534	0.946
1100.685	1.322
1268.655	1.588
1293.000	1.156
1316.662	1.358
1326.439	1.160
1375.116	1.319

The positions and intensities of peaks in this report were all identified with the Grams peak-picking algorithm and with no smoothing applied. The Grams algorithm uses a mathematical center-of-gravity computation (CG_X) to identify the position of the peak maximum.⁷

$$CG_X = X_1 + \frac{Y_2 - Y_1}{Y_2 - Y_3} \times \Delta X \quad (6)$$

where X_i denotes the wavelength or frequency of the data point adjacent to the selected peak, ΔX is the data spacing, and Y_n are the intensities of the data points in the vicinity of the peak. The center of gravity method has been shown to give satisfactory performance when compared with other peak-picking methods for evaluating the positions of peaks in polystyrene standards.⁸ When used to evaluate synthetically generated symmetrical Lorentzian peaks, the method was shown to yield values with an uncertainty $<0.01 \text{ cm}^{-1}$ at a signal-to-noise ratio (S/N) of 1000 and with an uncertainty $<0.7 \text{ cm}^{-1}$ at S/N of 20.⁹

Although the Grams algorithm uses a mathematical approach to identify the position of the peak maximum, the algorithm used to report the maximum peak intensity appears to be much simpler. (This was not explained in the user documentation.) The intensity reported in the peak table is the digitized value of the data point closest to the CG_X . When a digitized data point is close to the center-of-gravity of the peak, reporting the intensity of the data point closest to the CG_X will be close to the true maximum in most cases.

When the positions of the peaks in Table 4 (k values of GB) were examined, all the peaks in the K spectrum were shifted to higher frequencies with respect to the corresponding peaks in the k spectrum. Indeed, the peak near 837 cm^{-1} showed the maximum deviation in the position of a peak. The reported position was 836.843 cm^{-1} in the k spectrum and 836.968 cm^{-1} in the K spectrum. The shift in the peaks occurred as a result of the mathematical transformation of the spectrum in eq 1 as each point in the spectrum was multiplied by ν ($k \rightarrow K$) or divided by ν ($K \rightarrow k$). In the K spectrum, the transformation increased the relative intensities on the higher wavenumber side of the peak relative to the points in the k spectrum. The effect of this phenomenon can be clearly seen in Figure 6. The red trace in the figure is a synthetically generated symmetrical Lorentzian peak having both a peak maximum and a center of gravity at 1000.00 cm^{-1} . When the peak was converted to a k spectrum using eq 1, the resulting asymmetry shifted the center of gravity of the peak to 999.95 cm^{-1} , as seen in the blue trace.

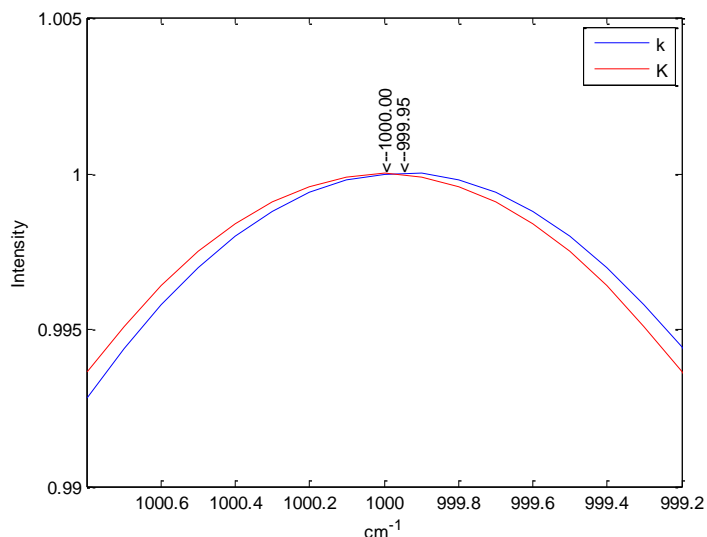


Figure 6. Lorentzian peak (full width at half height of 20 cm^{-1}) in a synthetically generated K spectrum (red trace), contrasted with the same peak in the k spectrum computed with eq 1 (blue trace). For this data, $CG_{X,K} = 1000.00\text{ cm}^{-1}$ and $CG_{X,k} = 999.95\text{ cm}^{-1}$.

The spectra were scaled to $Y_{max} = 1$.

The complex optical constants of a number of the standard chemical agents, including GB, were measured by researchers from PNNL and DPG, and the compiled data was distributed by PNNL in the form of an electronic database.^{2,3} A minimum of five and a maximum of seven samples of each agent were evaluated in cells with different path lengths. After correcting for the effects of Fresnel reflection from the cell windows, the pooled absorbance spectra were subjected to a weighted least-squares calculation to derive K values. Data points with absorbance (A) of >2.5 were given a weight of zero. The imaginary part of the refractive index of the agent was then derived through the K-K analysis of the resulting linear absorptivity coefficients.

The fingerprint regions of the complex refractive index of GB from ECBC and the PNNL database are shown in Figure 7. The positions and relative intensities of the peaks in the k spectra are similar. For the 13 strongest peaks within the full range of the spectra, the mean deviation in the peak positions ($\tilde{\nu}_{\text{ECBC}} - \tilde{\nu}_{\text{PNNL}}$) is only -0.27 cm^{-1} . The maximum fractional deviation in the values of the absorption index, expressed as $(k_{\text{PNNL}} - k_{\text{ECBC}})/(k_{\text{ECBC}} \times 100)$, is 12.1% for the P–F stretch near 836.8 cm^{-1} . Mean fractional deviation for the 13 peaks is 4.5%. The intensities of several of the absorption features in the spectrum of GB indicate that the absorption bands near the peak maxima may have been fitted with as few as two of the five path lengths in the study. According to Sharpe et al., cells were given a subjective letter grade from A to D, which was “based upon the quality of fringes from observation of empty cell spectrum,” and no other uncertainties in the determinations of the cell path lengths were given.² Cell path lengths were reported to the nearest $0.1 \text{ }\mu\text{m}$ (i.e., two significant figures for the cells with the shortest path lengths: 3.5 and $5.2 \text{ }\mu\text{m}$). For this reason, such a close agreement between the ECBC and PNNL data may be considered remarkable.

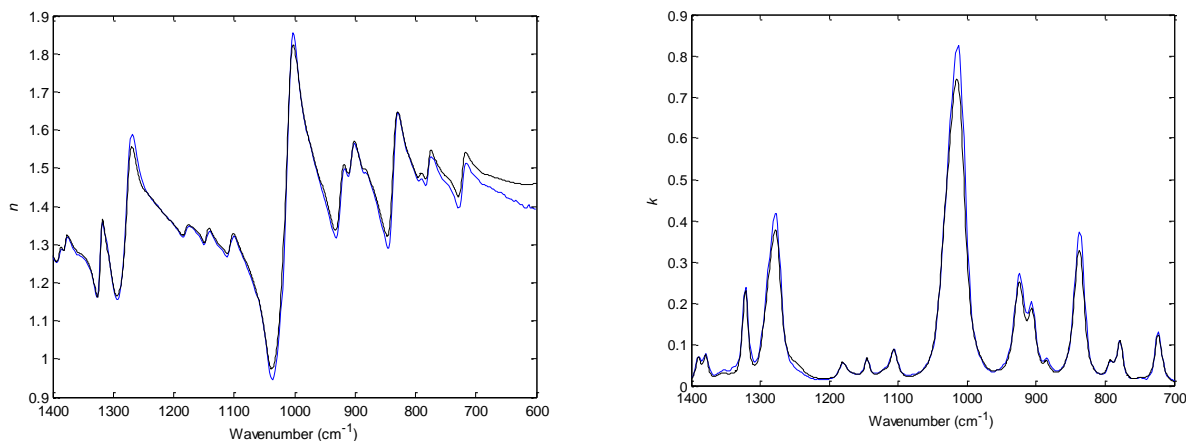


Figure 7. Complex refractive indices of GB from the ECBC (blue trace) and PNNL (black trace) databases. The spectra are qualitatively and quantitatively similar. A positive bias in the PNNL values of the real refractive index is seen near the low-frequency end of the range (600 cm^{-1}).

With the exception of the region below approximately 800 cm^{-1} , the values of the real refractive index from the ECBC and PNNL data for GB in Figure 7 are similar. At 4000 cm^{-1} , $n_{\text{ECBC}} = 1.367$ and $n_{\text{PNNL}} = 1.370$. Given that the K-K transform in the PNNL study was performed with $n(\infty)$ extrapolated from a single measurement of the refractive index at 589.3 nm , such a close agreement in real refractive indices appears to validate the method used to establish those anchor points for the OP nerve agents. From 800 to 600 cm^{-1} , the data exhibit a deviation that increases toward the lower-frequency end of the measured range in both sets of data. As noted previously, if a compound produces a spectrum with unobserved peaks below the cutoff, this can induce a positive bias in the calculated values of the real refractive index at frequencies near the cutoff.

In the 1960s, the optical properties of a number of chemical agents, including GB, were studied at SRI on dispersive instruments.¹ The compounds were measured using transmission in solution with a combination of carbon tetrachloride and carbon disulfide. The absorbance bands of those two solvents have little overlap. Combining sets of spectra in the two different solvents enabled the absorptivities of the agents to be obtained across the full-spectral range of the study. However, intermolecular interactions between solvent and solute can induce changes in the positions and intensities of absorption features when compounds are measured in solution. Nevertheless, the resulting data from SRI was useful for examining the k below the cutoff of the more current measurements from ECBC and PNNL. As shown in Figure 8, when the three sets of GB data in the region below 1000 cm^{-1} were plotted together, it was possible to observe several significant absorption features below 600 cm^{-1} . As shown in Figure 7, unobserved features in k can introduce errors into the K-K transformation, which then induce bias in n .

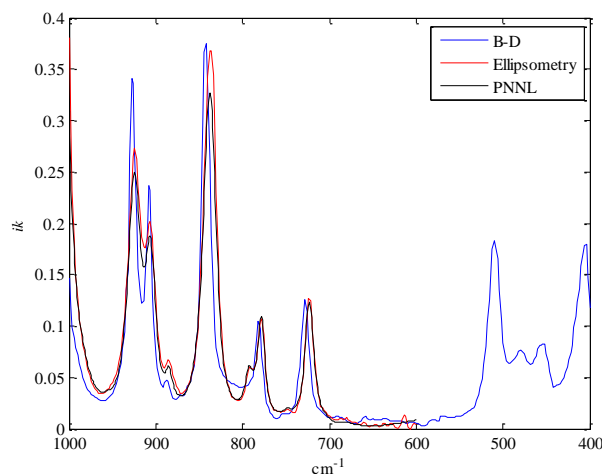


Figure 8. Imaginary refractive indices of GB from SRI (blue trace), ECBC (red trace), and PNNL (black trace) ellipsometry data. Note the presence of several absorption features at frequencies below 600 cm^{-1} in the SRI data. As shown in Figure 1, undetected peaks below the cutoff of the absorption index induce a positive bias in the lower-frequency values of n derived from a K-K transformation. Such an effect is likely responsible for the deviation in the lower-frequency values of the real refractive index of GB from the ECBC and PNNL data shown in Figure 7.

Analysts understand that there are inherent tradeoffs in choosing a particular analytical technique. As noted previously, the advantage of using the ellipsometric method to measure the optical constants of liquid compounds vis-à-vis the transmission method is the ability to acquire the optical constants in a single analysis. The direct acquisition of the real part of the refractive index, without the need to extrapolate a value of n well outside of its measured range to use as an anchor point, is particularly useful. On the other hand, the S/N of spectral data from ellipsometric measurements can be inherently lower than those obtained using transmission techniques. This is shown in Figure 9, which is an expanded view of the baselines in the fingerprint region of the GB absorption index spectra from ECBC and PNNL. The ellipsometer

spectrum is visibly noisier than the PNNL³ spectrum. Within the region from 2250 to 2150 cm^{-1} , where $k \approx 0$, the root mean square (RMS) noise is 1.0×10^{-4} in the ECBC spectrum and 1.5×10^{-5} in the PNNL spectrum.

Using the ellipsometry technique presents another disadvantage because it requires more than 4 h to acquire the full range of data needed to accurately reduce the measurements to complex optical constants, even at a spectral resolution of 4 cm^{-1} (compared with the 2 cm^{-1} resolution used for the PNNL data). With the ellipsometry technique, after the first test, the compound is typically left in the cell, and the cell is slightly adjusted in the z axis without removing the cell from the mount. The test is then repeated as a check for changes in birefringence. Completing both tests, including adjustments to the z axis, requires nearly 9 h. Although the Bomem spectrometer (ABB) in the ellipsometer can be used to achieve a higher spectral resolution than the 4 cm^{-1} used in the ECBC measurements, doing so without an increase in noise would also require a corresponding increase in the number of scans. Absorbance bands of the chemical agents in the liquid phase are generally broad, and a visual inspection of the spectra obtained from the two techniques shows little difference in the shapes of the peaks.

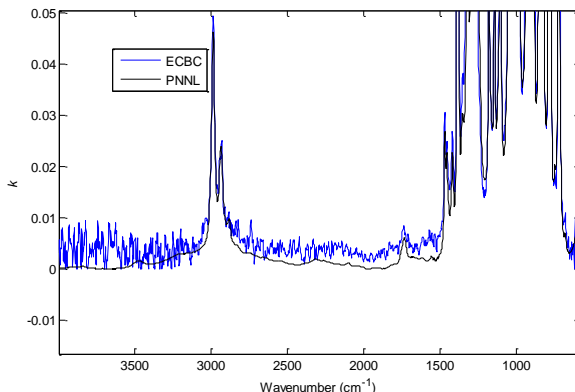


Figure 9. Baselines in k spectra of GB from ECBC (blue trace) and PNNL (black trace). Compared with the PNNL data, the ECBC spectrum is visibly noisier. For example, in the 2250 to 2150 cm^{-1} region, the RMS noise is 0.000015 in the PNNL spectrum and 0.00010 in the ECBC spectrum.

3.2 Complex Refractive Index of GF

The complex refractive index of GF is shown in Figure 10. Figure 11 shows the linear absorptivity coefficient of the compound, which was computed by rearranging eq 1. Values of k and K at selected peak maxima are given in Table 6. Values of the real refractive index at selected maxima and minima are shown in Table 7.

Figure 12 shows plots of the GF fingerprint regions in the optical constants obtained from the ECBC and PNNL data.³ As shown in this figure, the spectra are qualitatively and quantitatively similar. In contrast with the spectra of the real refractive index of GB, the

PNNL spectrum of GF exhibited little positive bias near 600 cm^{-1} relative to the ECBC data. This may be explained by the fact that the PNNL spectrum of GF was recorded with a lower limit of 450 cm^{-1} , and the K-K transformation included data from the low-frequency peaks absorption features. Both spectra show a real refractive index of 1.421 at 4000 cm^{-1} , which validates the method used by PNNL to determine the values of $n(\infty)$ for the nerve agents. A comparison of the ECBC and PNNL GF k spectra shows that the most intense features in the PNNL spectrum are 8 to 10% lower than the corresponding peaks in the ECBC spectrum. When considering the reported path lengths used to compute the k index, it appears that the peak maxima of the absorption features exhibiting the largest deviations from the ECBC data may have been computed using the absorbance data from only two of the five cells within those spectral regions. However, when the GF data were computed across the region 1500 to 600 cm^{-1} , the integrated area in the k spectrum from the PNNL database was only 2.5% lower than that of the ECBC spectrum. Furthermore, the mean deviation in the positions of the peak maxima of the 10 strongest peaks, computed as $\tilde{\nu}_{\text{ECBC}} - \tilde{\nu}_{\text{PNNL}}$, was only -0.120 cm^{-1} , which further demonstrates the similarity of the spectra.

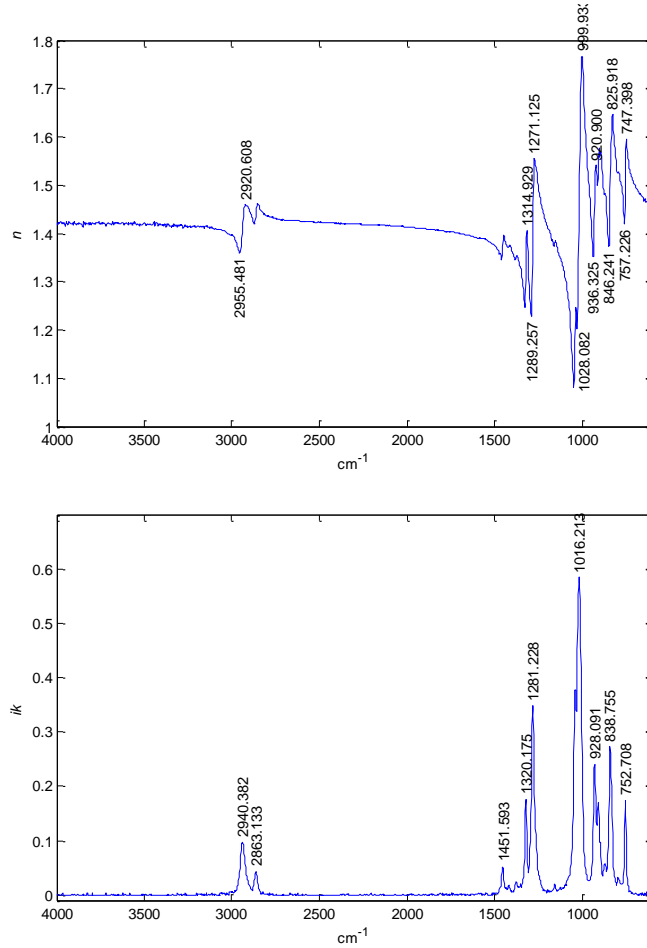


Figure 10. Complex refractive index of liquid GF: n (top) and k (bottom).

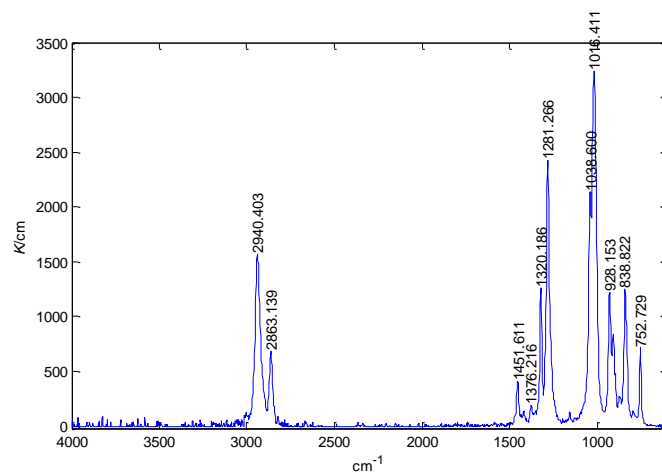


Figure 11. Linear absorptivity coefficient (K) of liquid GF.

Table 6. Positions and Intensities of Selected Peaks in k and K Spectra of GF

k		K	
cm^{-1}	Intensity	cm^{-1}	Intensity
752.708	0.1742	752.729	715.1
838.755	0.2725	838.822	1247.9
907.071	0.1698	907.122	839.9
928.091	0.2403	928.153	1216.8
1016.213	0.5838	1016.411	3238.3
1038.567	0.3770	1038.600	2136.3
1281.228	0.3472	1281.266	2426.8
1320.175	0.1756	1320.186	1265.8
1451.593	0.0510	1451.611	404.2
2863.133	0.0437	2863.139	682.9
2940.382	0.0978	2940.403	1569.7

Table 7. Positions and Values of Selected Maxima and Minima in Real Refractive Index of GF

Position (cm ⁻¹)	Intensity
747.398	1.595
757.226	1.420
825.918	1.646
846.241	1.372
911.473	1.499
920.900	1.541
936.325	1.352
999.933	1.766
1028.082	1.201
1034.768	1.247
1046.381	1.081
1271.125	1.555
1289.257	1.228
1314.929	1.405
1326.186	1.247
2920.608	1.460
2955.481	1.359

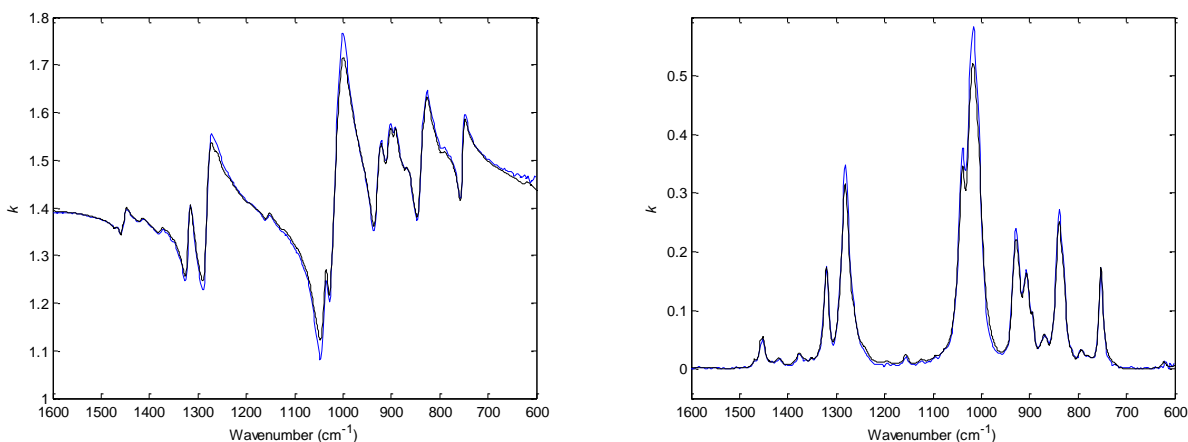


Figure 12. Complex refractive index of GF from ECBC (blue trace) and PNNL (black trace) databases. The spectra are qualitatively and quantitatively similar.

3.3 Complex Refractive Index of HD

The Bomem spectrometer (ABB) in the J.A. Woollam mid-IR ellipsometer used in this study was a Fourier transform instrument. This means that data sampling and digitization were done in the time domain. The mirror in the interferometer moved at a fixed rate, which meant that once the Fourier transform, phase-correction, and apodization functions were applied to the interferogram, the data points were evenly spaced in frequency.

By convention, the points on the mid-IR spectra x axis, which then represents frequency, are normally plotted with units of $\frac{1}{\lambda}$, where λ is the wavelength in centimeters and is labeled as either wavenumbers or reciprocal centimeters. The software that processed the raw data from the ellipsometer incorporated a feature that computed the S/N and varied the spacing of the values for Ψ and Δ that were written to the data file, which increased the spacing proportionally in regions where the S/N was lower. By default, this feature in the software was switched on. Early in this project, the optical constants of several materials were recorded with the software feature in the default mode. This resulted in optical constants with data intervals that were higher in the regions with the lowest S/N; in other words, in the high-frequency regions, where instrument noise was higher, the absorbance features tended to be weaker. Because only files from processed values of Ψ and Δ were written to disk, instead of the original interferograms, the raw inteferogram data are unrecoverable.

Among the compounds described in this report, the optical constants of HD were computed from data in which the variable-data-spacing feature was used. Figure 13 shows the data spacing of the spectra recorded by the ellipsometer software for these two compounds.

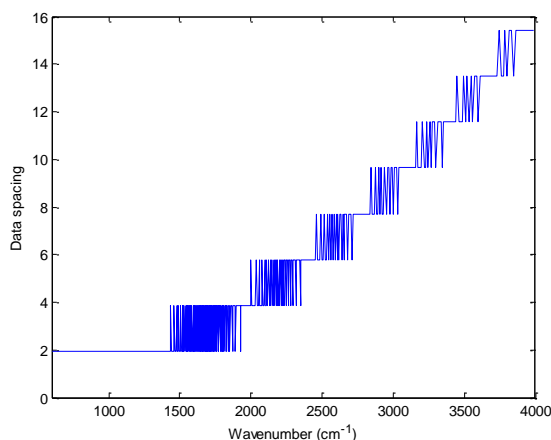


Figure 13. Data spacing in the Ψ and Δ of HD, as recorded by the ellipsometer software. The data spacing varied from 1.929 cm^{-1} at the low-frequency end of the data range to as high as 15.43 cm^{-1} near the high-frequency end of the data range (4000 cm^{-1}).

At the time of this study, the ECBC database of condensed-phase materials included at least three spectra of each compound with n and k values listed by wavenumber. For each optical constant, one file is written to a tab-delimited ASCII format with wavenumber values in the first column, the real refractive index in the second column, and the imaginary refractive index in the third column. In addition, the real and imaginary refractive indices are available in two separate files written in the Grams algorithm (.spc) format. Grams algorithm data files incorporate a compact binary format with extensive header information.

For compatibility with modern spectral-processing software, which generally accepted evenly spaced data files, the optical constant of HD was interpolated back to a data

spacing of 1.929 cm^{-1} using the Matlab Piecewise Cubic Hermite Interpolating Polynomial (pchip) switch with the interp1.m function (MathWorks; Natick, MA). According to the documentation of the function, the pchip algorithm, "...preserves the shape of the data and respects monotonicity."¹⁰ Use of the pchip tends to reduce data overshoots with rapidly changing data. When the interpolated data are viewed at full scale, little or no change in the shapes of the spectra may be seen. The effects of the interpolation become apparent only when the viewing area of the region is expanded. This is illustrated in Figure 14, which shows plots of the imaginary refractive index of HD before and after interpolation. The blue line traces the original variably spaced data, and the red line shows the results of the interpolation. When the HD spectra are viewed at full scale (the left side of the figure), the effects of the interpolation are not visible. The changes in the HD spectrum only become apparent when an interpolated region is expanded (right side of the figure). We note that for $\tilde{\nu} < 1460$, which encompasses all of the strongest absorption bands in the spectrum, only a single data point at 1438.791 cm^{-1} had to be interpolated. All data points within the remote sensing region (defined as $8\text{--}12\text{ }\mu\text{m}$) were recorded by the ellipsometer at a data spacing of 1.929 cm^{-1} .

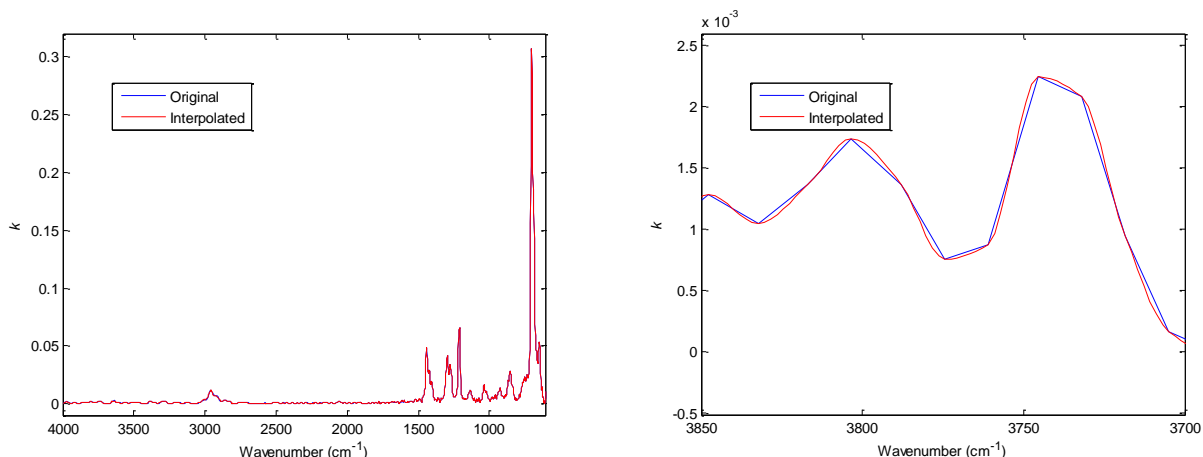


Figure 14. Imaginary refractive index of HD from ellipsometry measurements at ECBC: original data with variable spacing (blue trace) and spectrum after interpolating with the Matlab pchip algorithm (red trace).

The complex refractive index of HD is shown in Figure 15. Figure 16 shows the linear absorptivity coefficient of the compound, which was computed by rearranging eq 1. Values of k and K at selected peak maxima are given in Table 8. Values of the real refractive index at selected maxima and minima are shown in Table 9.

In contrast with the OP nerve agents, absorption features in the sulfur mustards are generally weaker. The strongest absorption band, near 702 cm^{-1} , arises primarily from C–Cl, with a smaller contribution from the C–S stretch.¹¹ With a k_{max} of 0.307, however, it is more than 2.5 times weaker than the strongest absorption feature in GB and only slightly more than one-half as intense as the strongest absorption feature in GF. The C–Cl/C–S band at 702 cm^{-1} is

outside of the remote-sensing window. Within the 8 to 12 μm region, the strongest feature, at 1210 cm^{-1} ($\text{S-CH}_2\text{ wag/Cl-CH}_2\text{ wag}^{11}$), exhibits $k_{\text{max}} = 0.065$.

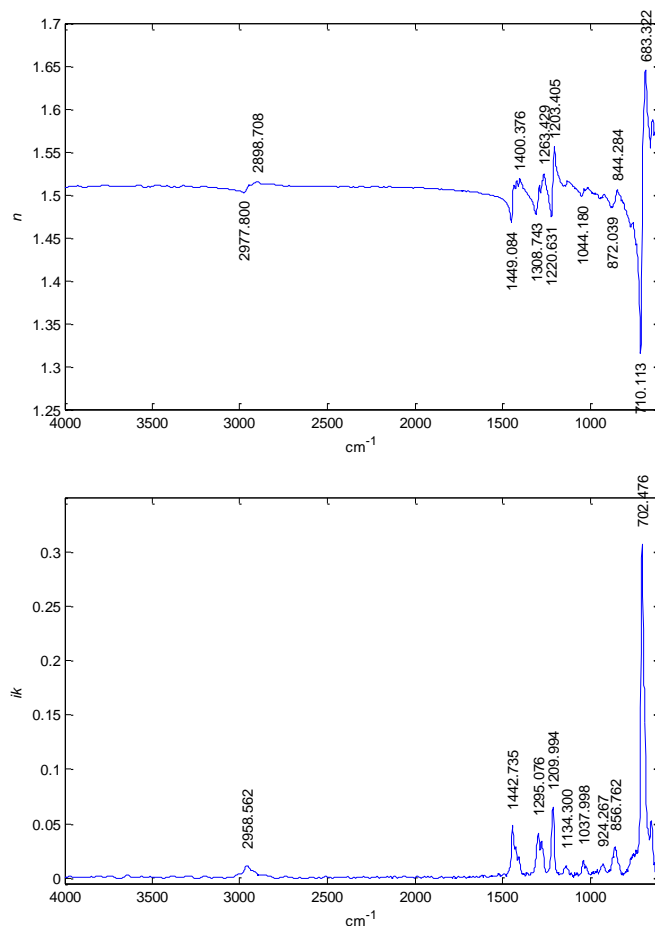


Figure 15. Complex refractive index of liquid HD: n (top) and k (bottom).

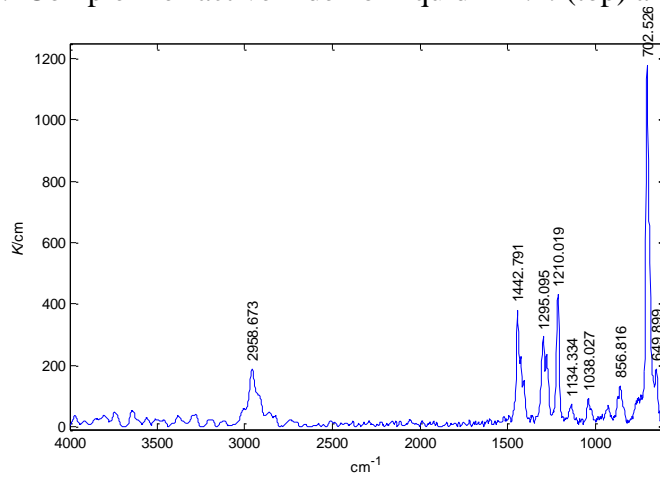


Figure 16. Linear absorptivity coefficient of liquid HD.

k		K	
cm^{-1}	Intensity	cm^{-1}	Intensity
649.683	0.05298	—	—
702.476	0.30740	702.526	1177.7
856.762	0.02834	856.816	132.4
924.267	0.01365	—	—
1037.998	0.01623	1038.027	91.9
1134.300	0.01145	1134.334	71.2
1209.994	0.06540	1210.019	431.6
1277.270	0.03370	1277.310	234.5
1295.076	0.04137	1295.095	292.2
1442.735	0.04803	1442.791	378.1
2958.562	0.01162	2958.673	187.7

—: no data

Table 9. Positions and Values of Selected Maxima and Minima in Real Refractive Index of HD

Position (cm^{-1})	Value
626.647	1.573
641.001	1.588
654.635	1.555
683.322	1.645
710.113	1.315
754.867	1.467
768.486	1.463
844.284	1.507
872.039	1.485
1044.180	1.498
1203.405	1.556
1220.631	1.474
1263.429	1.525
1281.623	1.503
1289.191	1.511
1308.743	1.477
1400.376	1.519
1417.746	1.516
1433.683	1.511
1449.084	1.468
2898.708	1.515
2977.800	1.502

Figure 17 shows the fingerprint region in the n and k spectra of HD from the ECBC and PNNL³ data. The k spectra are quantitatively and qualitatively similar. Similar to the

GB and GF, the values of the imaginary optical constant reported by PNNL appear to indicate that the least-squares fit of the HD absorbance data for the C–Cl/C–S feature in the vicinity of 702 cm^{-1} was probably computed using only the cells with the shortest two path lengths (11.0 and $16.0\text{ }\mu\text{m}$), which were assigned cell grades of D. The Type-A uncertainty reported by PNNL for the k values of HD was 2.4%, which reflected the statistical uncertainty in the least-squares fits of the absorbance spectra acquired to compute K . If measured data points from only two spectra were available to fit K values near 702 cm^{-1} , an estimate of the statistical uncertainty would not be possible unless the fit were forced to zero, which would then provide one degree of freedom (df ; where $df = n - 2$ and $n = 3$) for computing the Students- t distribution. With one degree of freedom, a confidence interval for a prediction of K would be computed as¹²

$$K(\tilde{\nu}) = K(\tilde{\nu}) \pm t_{0.025} \frac{s}{\sqrt{df}} \quad (7)$$

where $t_{0.025} = 12.7$ (from the Student's t table) and s is the estimated standard deviation. The standard deviation, resulting from two measurements of absorbance of these lines at path lengths of 11.0 and $16.0\text{ }\mu\text{m}$, would have to be multiplied by 12.7 to obtain a 95% confidence interval in the determination of K near 702 cm^{-1} . With $K_{\text{max}} \approx 0.061$ at 702 cm^{-1} , a statement encompassing uncertainty at that frequency would be: $K = 0.061 \pm 0.00146$. This means that the estimate of s would be $0.00146/12.7$ or 0.000115 , which is equal to approximately 0.19% of the value of K . When spectra have been obtained from different instruments, with differing frequencies of data points and spectral resolution, comparisons may be done by integrating across similar regions within the spectra. Such a comparison is shown in Table 10. Across the region of 1550 to 602 cm^{-1} , the integrated k values of the ECBC spectrum are 7.8% higher than those of the PNNL³ spectrum. Within the region encompassing the most intense features, 800 to 602 cm^{-1} , the ECBC spectrum is only 7.3% higher than the PNNL spectrum.

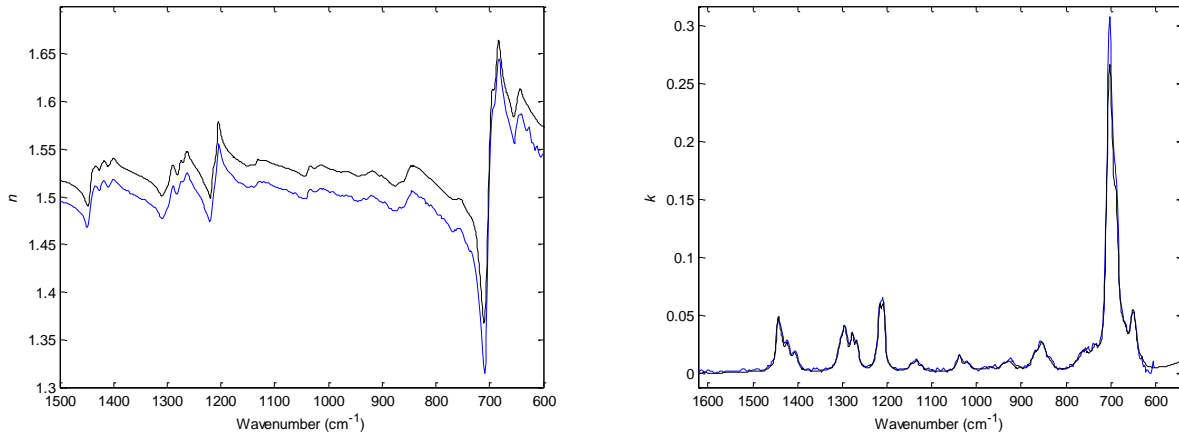


Figure 17. Complex refractive index of HD from ECBC (blue trace) and the PNNL database (black trace). The k spectra are qualitatively and quantitatively similar, while the traces of the real refractive index exhibit an offset: $n_{\text{ECBC}} - n_{\text{PNNL}} \approx 0.02$.

Table 10. Integrated Areas in k Index from PNNL and ECBC Measurements of HD

Region (cm^{-1})	Area		
	PNNL	ECBC	(PNNL-ECBC)/ ECBC
1550–602	17.141	18.596	–0.0782
800–602	9.605	10.359	–0.0728
1550–719	8.837	9.633	–0.0826

Note: The deviation, expressed as the fractional difference between the two spectra, was less than 10% within the spectral regions shown.

In contrast with the k spectra, the real refractive index spectra of HD from the two laboratories, shown in Figure 17, exhibit an offset, with $n_{\text{ECBC}} - n_{\text{PNNL}} \approx 0.02$ across the full range of the measurements. No analogs of the sulfur mustards with a range of known refractive index values were available, unlike the nerve agents, for which the value of n could be extrapolated to 8000 cm^{-1} using dispersion curves of several similar OP compounds. This meant that the K-K transformation was run using only a single measured value: 1.5318 at 589 nm.² As noted previously, ellipsometry can be used to measure both optical constants in a single measurement and eliminate the need to extrapolate the real part of the refractive index.

3.4 Complex Refractive Index of HN1

The complex refractive index of HN1 is shown in Figure 18. Figure 19 shows the linear absorptivity coefficient of the compound, which was computed by rearranging eq 1. Values of k and K at selected peak maxima are given in Table 11. Values of the real refractive index at selected maxima and minima are shown in Table 12.

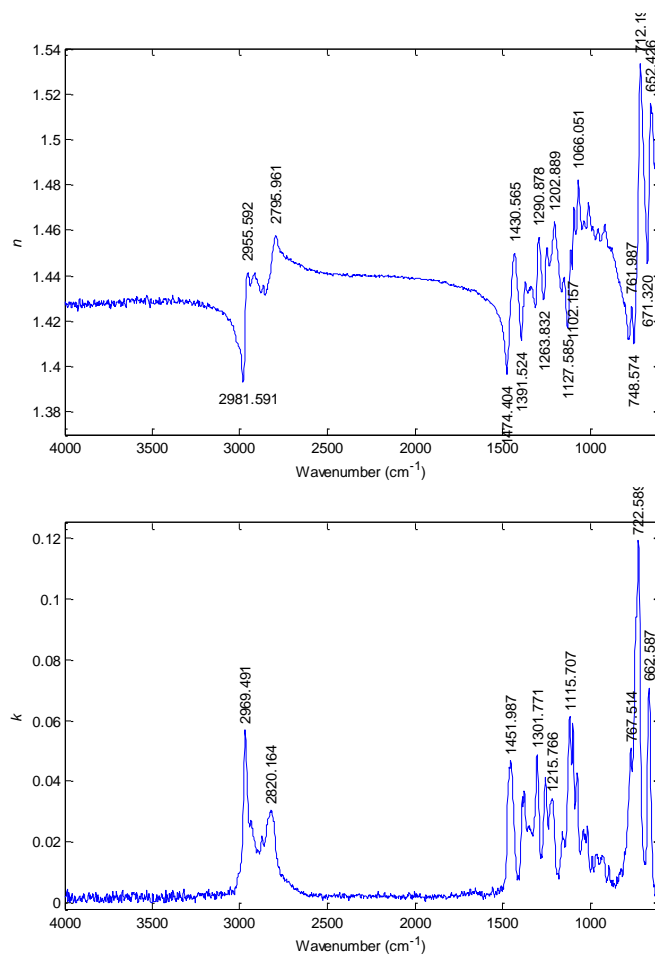


Figure 18. Complex refractive index of liquid HN1: n (top) and k (bottom).

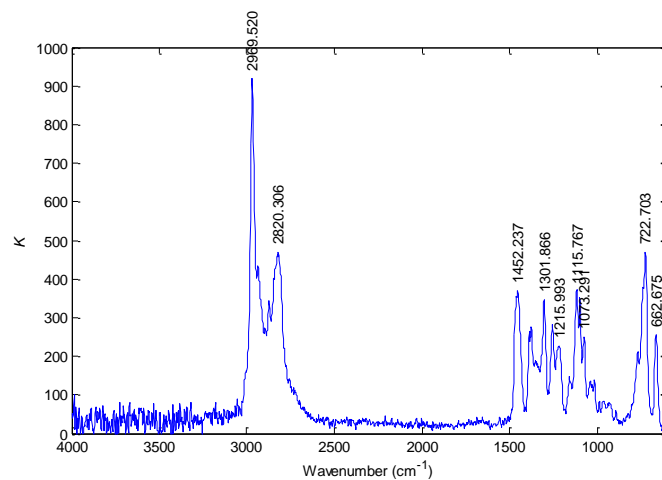


Figure 19. Linear absorptivity coefficient of liquid HN1.

Table 11. Positions and Intensities of Selected Peaks in k and K Spectra of HN1

k		K	
cm^{-1}	Intensity	cm^{-1}	Intensity
662.588	0.0708	662.675	256.2
722.589	0.1191	722.703	470.3
767.514	0.0509	1073.291	249.8
1073.250	0.0427	1097.066	352.8
1097.003	0.0589	1115.767	366.8
1115.707	0.0612	1215.993	227.7
1157.458	0.0234	—	—
1215.766	0.0344	—	—
1254.452	0.0410	1254.511	280.5
1301.771	0.0488	1301.866	346.9
1451.987	0.0467	1452.237	370.5
2820.164	0.0305	2820.306	469.6
2969.491	0.0567	2969.520	919.0

—: no data

Table 12. Positions and Values of Selected Maxima and Minima in Real Refractive Index of HN1

Position (cm^{-1})	Value
652.426	1.516
671.320	1.445
712.195	1.533
748.574	1.410
761.987	1.427
1066.051	1.482
1080.331	1.458
1091.355	1.470
1102.157	1.443
1109.760	1.452
1127.585	1.417
1202.889	1.464
1245.182	1.452
1263.832	1.429
1290.878	1.457
1313.100	1.426
1391.524	1.412
1430.565	1.449
1474.404	1.397
2795.961	1.458
2823.579	1.442
2955.592	1.441
2981.591	1.393

To our knowledge, the complex refractive index of HN1 has not been reported before this study. Assigning absorption features in tertiary amines to specific vibrational modes can be difficult.¹³ Hameka et al. performed a theoretical prediction of the infrared frequencies of a number of tertiary amines, including HN1 using a 3-21G method.¹⁴ Their results included correction factors for frequencies, as well as corresponding intensities. The authors assigned two absorption lines to C–Cl stretch, with corrected frequencies and intensities of 659 cm⁻¹ (intensity 73) and 651 cm⁻¹ (intensity 49). These absorption lines appeared to correspond to bands in our spectra that appeared at 723 and 663 cm⁻¹; therefore, we assigned these to the C–Cl asymmetric and symmetric stretches, respectively. Correlating other features in the fingerprint region of the *K* spectrum from the ECBC results to specific vibrational modes from Hameka et al. was more difficult. At frequencies greater than 800 cm⁻¹, Figure 19 shows a medium strong band at 1452 cm⁻¹. In aliphatic hydrocarbons, this would generally be assigned to a CH₃ umbrella mode,¹³ and HN1 has one methyl group. The closest computed frequencies, at 1449, 1450, 1450, and 1451 cm⁻¹, were assigned by Hameka et al. to the C–N bend, C–H bend, C–H bend, and C–N stretch, respectively. The feature probably arises from several vibrational modes. We concluded that no other bands in the *K* spectrum could be reliably correlated to the computed spectrum. Computers and spectral prediction algorithms have improved greatly since Hameka, et al. computed the spectrum of HN1, and rerunning the computations could be useful.

3.5 Complex Refractive Index of VX

The complex refractive index of VX is shown in Figure 20. Figure 21 shows the linear absorptivity coefficient of the compound, which was computed by rearranging eq 1. Values of *k* and *K* at selected peak maxima are given in Table 13. Values of the real refractive index at selected maxima and minima are shown in Table 14. The data points in ψ and Δ were recorded with even spacing, and the values of *n* and *k* were computed at a data spacing of 1.929 cm⁻¹ across the full range of the measurements.

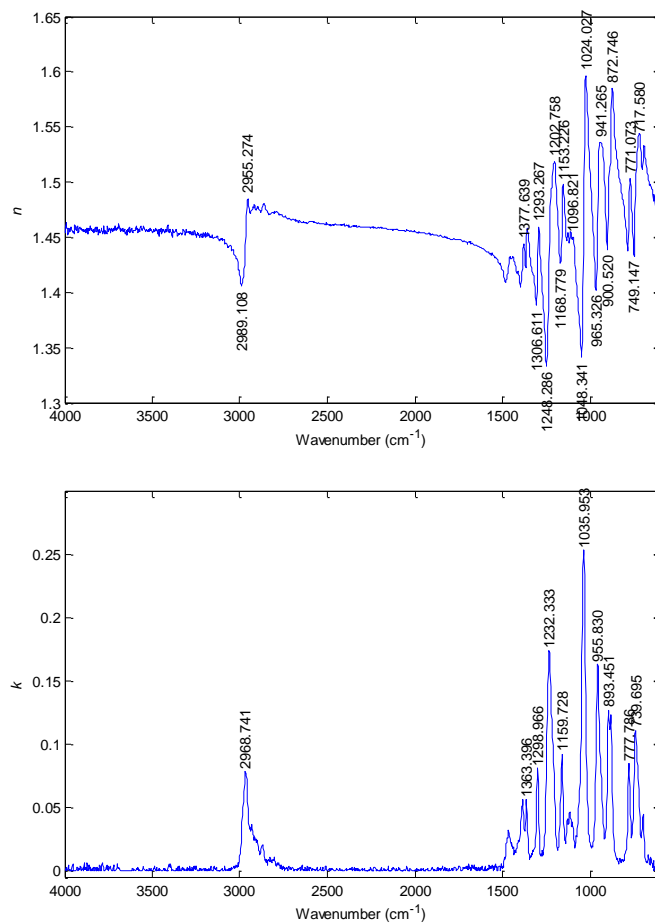


Figure 20. Complex refractive index of liquid VX: n (top) and k (bottom).

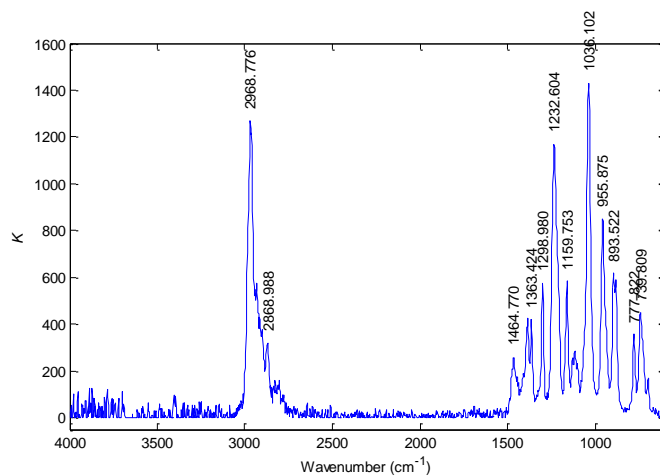


Figure 21. Linear absorptivity coefficient of liquid VX.

Table 13. Positions and Intensities of Selected Peaks in k and K Spectra of VX

k		K	
cm^{-1}	Intensity	cm^{-1}	Intensity
696.275	0.0445	—	—
739.695	0.1108	739.809	447.9
777.786	0.0844	777.822	358.1
880.417	0.1227	880.454	589.1
893.451	0.1268	893.522	618.0
955.830	0.1629	955.875	850.7
1035.953	0.2530	1036.102	1430.1
1159.728	0.0921	1159.753	582.5
1232.333	0.1738	1232.604	1169.2
1298.966	0.0813	1298.980	576.6
1363.396	0.0563	1363.424	419.0
1384.129	0.0560	1384.153	422.9
—	—	1464.770	257.8
—	—	2868.988	320.9
2968.741	0.0784	2968.776	1269.9

—: no data

Table 14. Positions and Values of Selected Maxima and Minima in Real Refractive Index of VX

Position (cm^{-1})	Value
633.431	1.4887
691.726	1.5329
717.580	1.5443
749.147	1.4330
771.073	1.5028
783.934	1.4375
872.746	1.5848
900.520	1.4390
941.265	1.5359
965.326	1.4023
1024.027	1.5959
1048.341	1.3414
1096.821	1.4501
1153.226	1.4976
1168.779	1.4268
1202.758	1.5185
1248.286	1.3332
1293.267	1.4594
1306.611	1.3889
1358.293	1.4581
1377.639	1.4435
2955.274	1.4845
2989.108	1.4060

The complex refractive index of VX was previously reported by PNNL.³ Figure 22 shows the n and k spectra of the compound from ECBC and PNNL. The real refractive index of the spectra exhibits an offset that varies by wavenumber. Across much of the spectral range, the values of the refractive index from ECBC were lower than those reported by Sharpe et al.² Near the long wavelength end of the spectra (e.g., at 600 cm^{-1}), $n_{\text{PNNL}} - n_{\text{ECBC}} \approx 0.07$. Much of the relatively large bias near the lower frequency cutoff of the PNNL spectrum may be attributable to the fact that, at least according to Barrett et al.,¹ VX has a moderately strong band at 527 cm^{-1} that influences the magnitude of the refractive index at higher frequencies. As described in Section 1 and illustrated in Figure 1, these effects could not be captured by the spectra used in the K-K transformation of the real part of the refractive index, which were limited to 600 cm^{-1} .

The k spectra are generally qualitatively similar, although the PNNL spectrum exhibits a weak feature at 1617 cm^{-1} that may indicate the presence of an impurity. The stated purity of the VX, used to generate the n and k spectra for the PNNL database, was reported as 93.1%. Therefore, it is certainly possible that some of the small qualitative differences in the spectra from the two laboratories may be attributable to differences in the composition of the starting materials. Within the region 1540 to 610 cm^{-1} , which encompasses most of the fundamental vibrations of the VX molecule, the integrated area in the k spectrum from ECBC is 42.1, and in the PNNL spectrum, the integrated area is 54.5. This is the largest quantitative difference reported for the chemical agents in this report. Much of the quantitative difference in the integrated areas of the two spectra may be largely attributable to differences in their baselines. This effect can be seen when a region is expanded to permit the baselines in the spectra to be examined more closely, as shown in Figure 23. The absolute differences in the peak maxima are very similar to the absolute differences of the valleys on either side of the peaks.

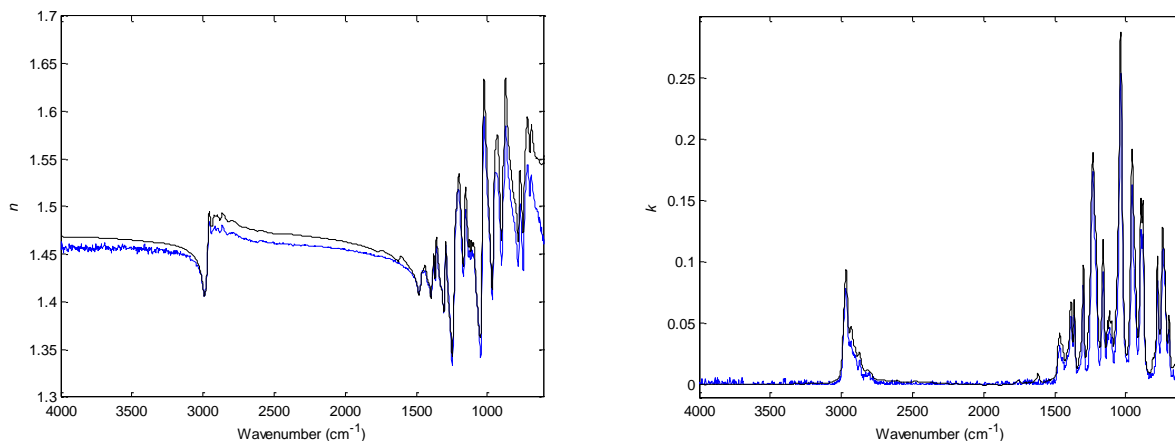


Figure 22. Complex refractive index of VX from ECBC (blue trace) and the PNNL database (black trace). The k spectra are qualitatively similar, and the traces of the real refractive index exhibit an offset.

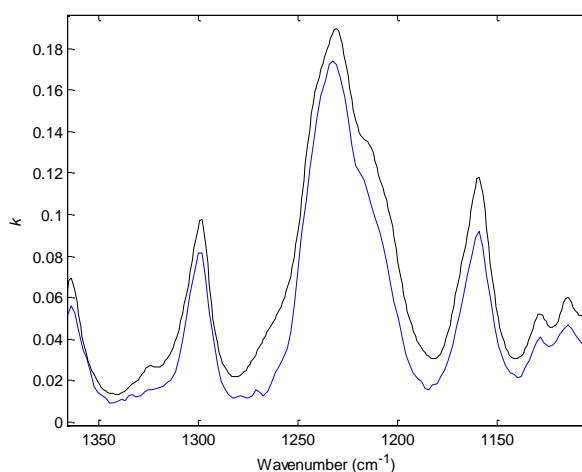


Figure 23. Imaginary refractive index of VX from ECBC (blue trace) and the PNNL database (black trace) expanded to the region near 1300 cm^{-1} . The expanded view shows that the PNNL spectrum exhibits a positive shift in the baseline relative to the ECBC spectrum.

4. CONCLUSIONS

We have measured the complex optical constants ($\hat{n} = n + ik$) of a variety of nerve agents and vesicants in the mid-IR spectra. The measurements were made using IR-VASE. Using ellipsometry with ATR permitted the determination of both optical constants in a single measurement. This is in contrast with the more traditional methods of obtaining the optical constants using transmission measurements that require the real refractive index to be extrapolated outside of the measured range. These ECBC results have shown that ellipsometry greatly improves upon the traditional transmission methods of acquiring the optical constants for the determination of the real part of the complex refractive index.

Blank

LITERATURE CITED

1. Barrett, W.J.; Dismukes, E.B.; Powell, J.B. *Infrared Studies of Agents and Field Contaminants: Second Annual Report, October 1968 through September 1969*; Contract No. DAAA15-68-C-0154; Southern Research Institute: Birmingham, AL, 1969; UNCLASSIFIED Report (AD506023).
2. Sharpe, S.W.; Johnson, T.J.; Thomas, H.; Dvorak, T.; Pagan, M. *Refractive Indices (1.5 to 20 μm) of Liquid Phase Chemical Warfare Agents: GA, GB, GD, GF, VX, EA 1699, HD, HN3, and L*; PNNL-14902; Pacific Northwest National Laboratory: Richland, WA, 2004.
3. DPG/NGA/DOE-CWA Library V2.0; [DVD-ROM]; Pacific Northwest National Laboratory, Richland, WA, January 2005.
4. Ohta, K.; Ishida, H. Comparison among Several Numerical Integration Methods for Kramers-Kronig Transformation. *Appl. Spectrosc.* **1988**, 42, 952–957.
5. Stenzel, O. *Das Dunnschichtspektrum*; Springer-Verlag: Berlin, Germany, 1996.
6. *Potential Military Biological/Chemical Agents and Compounds*; Army Field Manual 3-11.9; Department of the Army: Washington, DC, January 2005; UNCLASSIFIED Manual.
7. Grams/AI; Version 9.00 R2; Thermo-Fisher Scientific: Waltham, MA, 2009.
8. Hanssen, L.M.; Zhu, C. Wavenumber Standards for Mid-Infrared Spectroscopy. In *Handbook of Vibrational Spectroscopy*; Chalmers, J.M. and Griffiths, P.R., Eds.; John Wiley & Sons: Chichester, UK, 2002.
9. Cameron, D.G.; Kauppinen, J.K.; Moffatt, D.G.; Mantsch, H.H. Precision in Condensed Phase Vibrational Spectroscopy. *Appl. Spectrosc.* **1982**, 36, 245–250.
10. *MATLAB: The Language of Technical Computing, Using MATLAB, Version 6*; The Mathworks: Natick, MA, 2002.
11. Person, W.B.; Willis, B.; Kubulat, K.; Sosa, C.; Bartlett, R.J. Interpretation of Infrared Spectra of Chemical Agents (AD-P200672). In *Proceedings of the U.S. Army Chemical Research, Development and Engineering Center Scientific Conference on Chemical Defense Research*, 17–20 November 1987. U.S. Army Chemical Research, Development, and Engineering Center: Aberdeen Proving Ground MD, 1990; UNCLASSIFIED Report (ADB121449).
12. Paulson, D.S. *Applied Statistical Designs for the Researcher*, Marcel Dekker, Inc.: New York, 2003.

13. Colthup, N.B.; Daly, L.H.; Wiberley, S.E. *Introduction to Infrared and Raman Spectroscopy*; 3rd ed.; Academic Press Division of Harcourt Brace & Company: San Diego, CA, 1990.

14. Hameka, H.F.; Famini, G.R.; Jensen, J.O.; Jensen, J.L. *Theoretical Prediction of Vibrational Infrared Frequencies of Tertiary Amines*; CRDEC-CR-101; Chemical Research, Development, and Engineering Center: Aberdeen Proving Ground, MD, 2001; UNCLASSIFIED Report (ADA232880).

ABBREVIATIONS

ATR	attenuated total reflection
CAS RN	Chemical Abstracts Service Registry Number
CG_x	computed center of gravity
DPG	Dugway Proving Ground
DTGS	deuterated triglycine sulfate
ECBC	U.S. Army Edgewood Chemical Biological Center
FW	formula weight
GB	sarin, isopropyl methylphosphonofluoridate (agent)
GF	cyclosarin, cyclohexyl methylphosphonofluoridate (agent)
HD	distilled mustard, bis-(2-chloroethyl) sulfide (agent)
HN1	nitrogen mustard, bis-(2-chloroethyl)ethylamine (agent)
ik	imaginary part of the refractive index (dimensionless)
IR	infrared
IR-VASE	infrared variable angle spectral ellipsometer
k	absorption index (or extinction coefficient)
K	linear absorption coefficient
K-K	Kramers-Kronig
MCT	mercury–cadmium–telluride
n	real refractive index
OP	organophosphorous
pchip	Piecewise Cubic Hermite Interpolating Polynomial (Matlab from MathWorks)
PNNL	Pacific Northwest National Laboratory

PTFE	polytetrafluoroethylene
RCE	rotating-compensator ellipsometer
RMS	root mean square
SKK	subtractive Kramers-Kronig
S/N	signal-to-noise ratio
SRI	Southern Research Institute
VP	vapor pressure
VX	<i>O</i> -ethyl- <i>S</i> -(2-diisopropylaminoethyl) methylphosphonothioate (agent)

